Dalton Transactions

ROYAL SOCIETY OF CHEMISTRY

PAPER

View Article Online
View Journal | View Issue

Cite this: *Dalton Trans.*, 2025, **54**, 17941

Synthesis and SHG properties of the melamine-based material $(C_3N_6H_7)ZnX_3(C_3N_6H_6)$ (X = Cl, Br)

Melena Groß, [a] Catharina Darine Brand, [a] Patrick Schmidt, [a] Tim Parker, [b] Dai Zhang, [b] Carl P. Romao [c] and Hans-Jürgen Meyer *[a]

Received 19th September 2025,
Accepted 31st October 2025

DOI: 10.1039/d5dt02245b

rsc.li/dalton

The zinc halide–melamine system was investigated by conducting exploratory solid-state reactions and hydrothermal syntheses, yielding $Zn_3(OH)_2Cl_4(C_3N_6H_6)_3$ and $(C_3N_6H_7)ZnX_3(C_3N_6H_6)$ with X = Cl and Br. All compounds were characterized by single-crystal X-ray diffraction, revealing that there are two modifications of the melaminium–zinc-chloride–melamine compound, crystallizing with non-centrosymmetric space groups ($Pna2_1$ and $P2_1$). The presence of delocalized π-electron systems in compounds containing cyclic $(B_3O_6)^{3-}$, $(C_3N_3O_3)^{3-}$, or melamine derivatives is known to give rise to significant second harmonic generation (SHG) properties, provided that the given structure has no inversion center. All crystal structures feature Zn^{2+} in a tetrahedral coordination environment, forming layered structures. Spectroscopic measurements on phase-pure orthorhombic $(C_3N_6H_7)ZnBr_3(C_3N_6H_6)$ resulted in direct and indirect band gaps of 4.74 eV and 4.46 eV respectively. Measurements of the nonlinear optical response performed on single crystals of three different compounds revealed significant intensities following the sequence monoclinic $(C_3N_6H_7)ZnCl_3(C_3N_6H_6)$ > orthorhombic $(C_3N_6H_7)ZnBr_3(C_3N_6H_6)$ > orthorhombic $(C_3N_6H_7)ZnCl_3(C_3N_6H_6)$. Their SHG properties are compared with those of KTP, one of the most widely used SHG materials.

Introduction

Nonlinear optical (NLO) materials have garnered significant interest due to their important roles in optoelectronic applications, including frequency conversion, optical data storage, and photonics.[1] A cornerstone of second-order nonlinear optical phenomena, such as second-harmonic generation (SHG), is the requirement for non-centrosymmetric structures, which enable the macroscopic polarization needed for these processes.[2] Cyanurate-based systems, built upon the $(C_3N_3O_3)^{3-}$ ion, have emerged as promising building blocks for NLO materials.[3] These planar, π-conjugated units, isoelectronic with $(B_3O_6)^{3-}$ in β-BaB_2O_4 (BBO), display high polarizability and have demonstrated good SHG efficiencies in alkaline earth and rare-earth compounds.[3] Previous works, such as the syntheses of $Sr_3(C_3N_3O_3)_2$ and $Ca_3(C_3N_3O_3)_2$, have shown that such frameworks can adopt non-centrosymmetric arrangements and exhibit significant optical responses, making them strong candidates for practical applications.[4] However, further extending these concepts to organic–inorganic systems has proven challenging. Melamine $(C_3N_6H_6)$ shares structural similarities with cyanurate and offers great potential for NLO applications.[5] Its delocalized electron system and rich chemical versatility enable it to form complex frameworks with enhanced polarizability.[6] Unfortunately, melamine's inherent tendency to crystallize in centrosymmetric configurations often suppresses its utility for SHG applications.[7] To circumvent this limitation, strategies such as incorporating melamine into inorganic structures and leveraging secondary building units have been explored.[8] Recent studies on melamine-based metal halides, for example, have highlighted the potential for achieving non-centrosymmetric structures by combining heavy metal cations, such as Hg^{2+}, with melamine.[8a] While mercury may initially seem like a promising candidate due to its high polarizability and ability to induce structural asymmetry, its toxicity significantly limits its practical applications. This highlights the importance of exploring less hazardous metals to develop environmentally safer NLO materials for broader applications.

Zinc is a particularly promising candidate for SHG-active materials due to several key properties. Zinc ions (Zn^{2+}), belonging to the d^{10} electronic configuration family, exhibit high polarizability, which is a crucial factor in enhancing SHG

[a]*Section of Solid State and Theoretical Inorganic Chemistry, Institute of Inorganic Chemistry, Eberhard Karls University Tübingen, Auf der Morgenstelle 18, 72076 Tübingen, Germany. E-mail: juergen.meyer@uni-tuebingen.de*
[b]*Institute of Physical and Theoretical Chemistry, Eberhard Karls University Tübingen, Auf der Morgenstelle 15, 72076 Tübingen, Germany*
[c]*Department of Materials, Faculty of Nuclear Sciences and Physical Engineering, Czech Technical University in Prague, Trojanova 13, Prague 120 00, Czech Republic*

efficiency.[9] Additionally, Zn^{2+} ions readily form diverse coordination geometries, enabling structural flexibility that facilitates the adoption of non-centrosymmetric arrangements in crystal lattices.[10] Compounds incorporating Zn^{2+}, such as ZnO and its derivatives, have already demonstrated strong nonlinear responses and broad transparency ranges in the ultraviolet (UV) to visible spectrum.[11] Furthermore, zinc-based materials often show robust stability and processability, making them practical candidates for SHG applications.[12]

We conducted an exploratory study combining Zn^{2+} and melamine using solid-state and hydrothermal routes. This yielded a series of zinc–melamine compounds, some of which exhibit significant second-harmonic generation (SHG). These findings highlight melamine (Mel) as an effective ligand platform for the development of high-performance second-order nonlinear optical (NLO) materials.

Results and discussion

Syntheses

The hydrothermal reaction of $ZnCl_2$ and melamine in a Teflon-lined autoclave at 110 °C yielded two compounds: $Zn_3(OH)_2Cl_4(Mel)_3$, which contains melamine (Mel) as a ligand, and (MelH)$ZnCl_3$(Mel), which contains melamine as a ligand and melaminium (MelH) as a counter cation. A corresponding reaction with $ZnBr_2$ yielded (MelH)$ZnBr_3$(Mel) only.

The crystal structures of (MelH)$ZnCl_3$(Mel) and (MelH)$ZnBr_3$(Mel) were refined isotypically to crystallize in the non-centrosymmetric orthorhombic space group $Pna2_1$. The lattice parameters of the bromide containing compound are only slightly expanded compared to the chloride compound, due to the larger ionic radius of bromide (Table 1). The composition of the bromide compound was confirmed by combustion analysis (H = 2.35% ± 0.157%) and EDX (Zn : Br = 1 : 3.0(1)).

A similar mercury compound $(C_3N_6H_7)(C_3N_6H_6)HgCl_3$ has been already reported with the space group $Pna2_1$ and highlighted for its SHG properties.[8a] And finally a zinc compound $(H_7C_3N_6)(H_6C_3N_6)ZnCl_3$ obtained *via* hydrothermal synthesis has been reported to crystallize in the monoclinic space group $P2_1$.[8b] This compound did not form under the hydrothermal conditions that were previously used, but it was synthesized by solid-state reactions of $ZnCl_2$, melaminium hydrochloride, and melamine in a 1 : 1 : 1 molar ratio at 120 °C. The crystal structures and SHG properties of the compounds are reported as follows.

Structure of $Zn_3(OH)_2Cl_4(Mel)_3$

Single-crystal X-ray diffraction studies revealed that $Zn_3(OH)_2Cl_4(Mel)_3$ crystallizes in the triclinic space group $P\bar{1}$. The crystal structure is composed of three distinct zinc atoms interconnected by hydroxide groups. Each zinc atom adopts a distorted tetrahedral coordination geometry, featuring a mixed ligand environment comprising chloride, hydroxide, and melamine ligands (see Fig. 1). Zn1 and Zn3 are coordinated by two chloride ions, one hydroxide group, and one melamine ligand, bonded through an inner nitrogen atom. Zn2 is coordinated by two hydroxide groups and two melamine ligands, with each also bonded *via* inner nitrogen atoms (see Fig. 1).

Table 1 Summary of single-crystal data for (MelH)$ZnCl_3$(Mel) ($P2_1$ and $Pna2_1$), (MelH)$ZnBr_3$(Mel) ($Pna2_1$), and $Zn_3(OH)_2Cl_4(Mel)_3$ from structure refinements

	Compound			
	(MelH)$ZnCl_3$(Mel)		(MelH)$ZnBr_3$(Mel)	$Zn_3(OH)_2Cl_4(Mel)_3$
CCDC	2478821	2407677	2438541	2407380
Formula	$C_6H_{13}N_{12}Cl_3Zn$		$C_6H_{13}N_{12}ZnBr_3$	$C_{12}H_{26}Cl_4N_{24}O_2Zn_3$
Formula weight/g mol^{-1}	425.004	425.00	558.38	876.498
Density/g cm^{-3}	1.911	1.914	2.374	2.013
Z	2	4	4	2
Crystal system	Monoclinic	Orthorhombic	Orthorhombic	Triclinic
Space group	$P2_1$	$Pna2_1$	$Pna2_1$	$P\bar{1}$
a/Å	9.3366(2)	12.1055(4)	12.1482(2)	10.5358(1)
b/Å	6.6582(2)	18.3525(5)	18.8376(3)	10.5807(1)
c/Å	12.1344(3)	6.6402(2)	6.8263(1)	13.8676(2)
α/°	90	90	90	72.481(1)
β/°	101.703(2)	90	90	79.260(1)
γ/°	90	90	90	89.968(1)
V/Å^3	738.65(3)	1475.238(8)	1562.15(4)	1445.83(3)
T/K	150.0(1)	150.0(2)	150.0(1)	150.0(2)
Radiation type	Cu-K$_\alpha$	Cu-K$_\alpha$	Cu-K$_\alpha$	Cu-K$_\alpha$
Reflections measured	15 504	13 315	58 528	46 915
Independent reflections	2767	2486	3394	5911
Abs. coeff. (mm^{-1})	7.482	7.493	11.347	6.874
Goof (F^2)	1.0571	1.041	1.093	1.0933
R_{int}	0.0378	0.0419	0.0230	0.0310
R_1	0.0253	0.0367	0.0200	0.0172
wR_2	0.0584	0.0926	0.0590	0.0422
Flack	−0.009(8)	0.04(3)	−0.02(1)	—

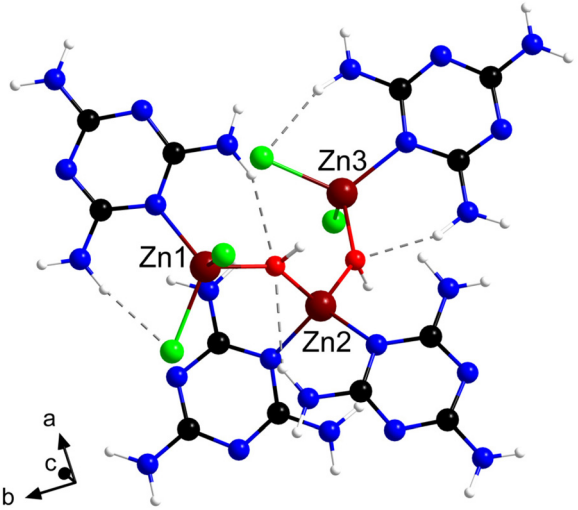

Fig. 1 Section of the crystal structure of $Zn_3(OH)_2Cl_4(Mel)_3$, with a central trinuclear arrangement of zinc atoms, interconnected *via* hydroxide bridges. Each zinc atom adopts a distorted tetrahedral environment surrounded by chloride, hydroxide, and melamine ligands.

Structure of orthorhombic and monoclinic (MelH)$ZnCl_3$(Mel)

The structure of orthorhombic (MelH)$ZnCl_3$(Mel) crystallizes in the non-centrosymmetric orthorhombic space group $Pna2_1$ (Fig. 2). The zinc atom in the structure is coordinated by three halide ligands and one melamine molecule through an inner nitrogen atom, forming the $(ZnCl_3Mel)^-$ anion with a distorted tetrahedral coordination geometry, with d_{Zn-N} = 2.031(1)–2.045 (1) Å, d_{Zn-Cl} = 2.2458(4)–2.3151(3) Å and d_{Zn-O} = 1.925(1)–1.947 (1) Å. In addition, a protonated melamine molecule is incorporated for charge compensation.

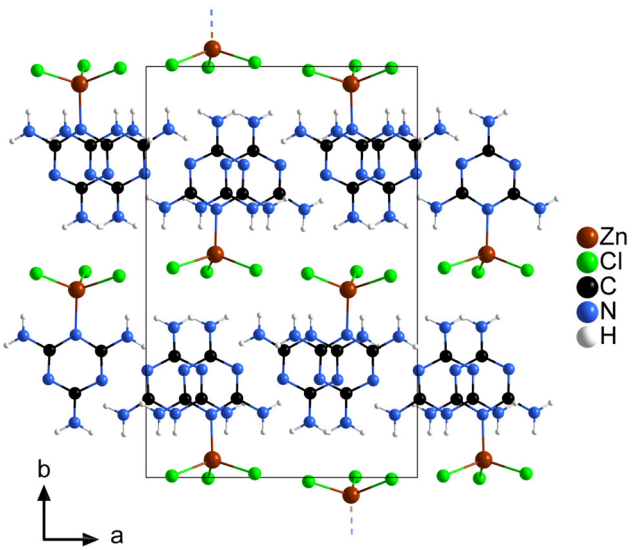

Fig. 2 Crystal structure of orthorhombic (MelH)$ZnCl_3$(Mel) showing the layered character of the structure.

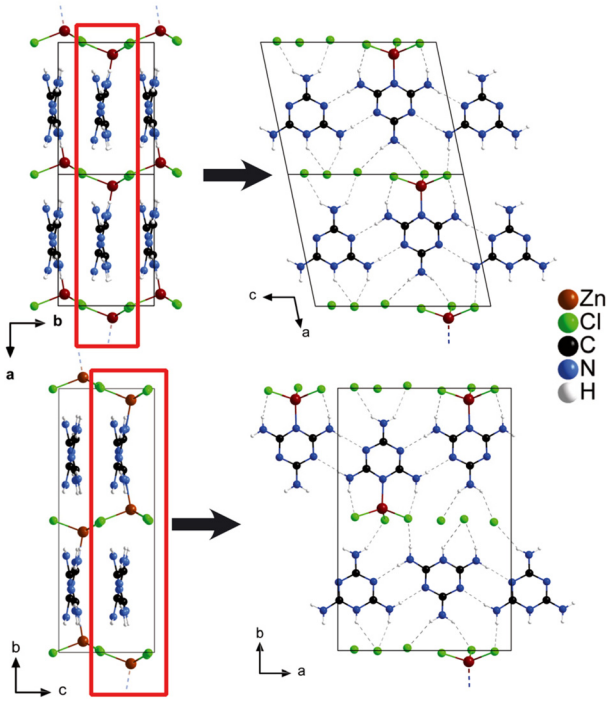

Fig. 3 Two views of the monoclinic (top) and orthorhombic (bottom) modifications of (MelH)$ZnCl_3$(Mel). The red box marks the section of the structure shown in the parent projections on the right.

These moieties together form a layered arrangement, most importantly with a stacking of melamine and melaminium along the polar *c*-axis. When viewed along the *a* direction, both melamine and melaminium are slightly tilted relative to each other (see Fig. 3, left side).

The structure of monoclinic (MelH)$ZnCl_3$(Mel) crystallizes in the non-centrosymmetric monoclinic space group $P2_1$ with d_{Zn-N} = 2.053(2) Å and d_{Zn-Cl} = 2.716(7)–2.2633(6) Å, which are in good agreement with the literature.[8b] Herein, the $(ZnCl_3Mel)^-$ and melaminium ions show different distributions in the structure, compared to the orthorhombic structure, as visualized in Fig. 3. These different arrangements are most likely a result of competing stabilizations of these structures *via* hydrogen bonding, with hydrogen bonding highlighted in Fig. 3 (right); see Tables S1–S4 for the complete list. A list of all distances surrounding the zinc atoms is provided for all compounds in Table S5. Most importantly, the melamine-based ring systems are stacked along the polar *b*-axis.

NLO measurements

Second harmonic generation (SHG) is a second-order nonlinear optical process in which two photons combine within a material to produce a new photon with twice the energy and half the wavelength of the incident light. This phenomenon arises from the interaction between the electromagnetic field and the material's nonlinear polarization.[13] To evaluate the SHG efficiency of the orthorhombic compounds (MelH)ZnX_3(Mel) (X = Cl, Br), measurements were conducted on

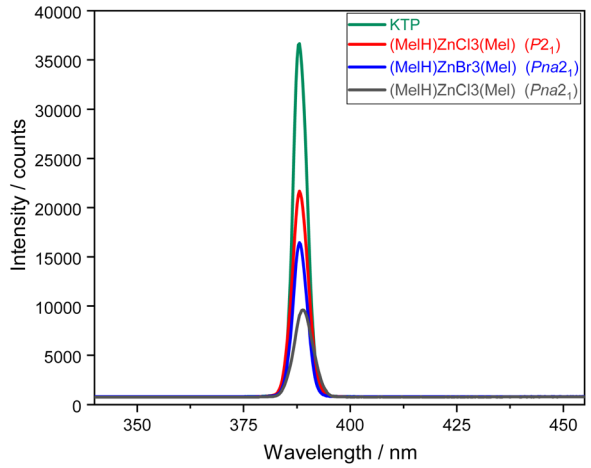

Fig. 4 Nonlinear optical spectra of KTP (green), monoclinic (MelH)$ZnCl_3$(Mel) ($P2_1$; red), orthorhombic (MelH)$ZnBr_3$(Mel) ($Pna2_1$; blue) and orthorhombic (MelH)$ZnCl_3$(Mel) ($Pna2_1$; grey) are shown for an excitation power of 5 mW. The only detectable signal is the SHG peak, which is located at approximately 390 nm.

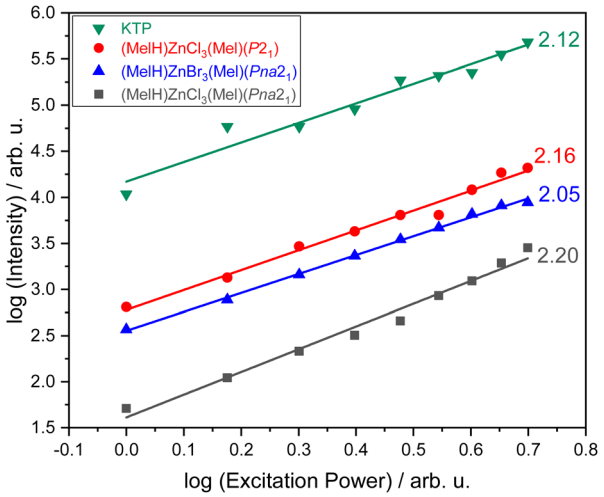

Fig. 5 Nonlinear optical spectra of KTP (green), monoclinic (MelH)$ZnCl_3$(Mel) ($P2_1$; red), orthorhombic (MelH)$ZnBr_3$(Mel) ($Pna2_1$; blue) and orthorhombic (MelH)$ZnCl_3$(Mel) ($Pna2_1$; grey). The excitation power dependence of the SHG signal is presented on a double logarithmic scale. Continuous lines represent the corresponding linear fits, with slopes derived from the fitted data.

single crystals using a custom-designed confocal microscope, as described in the Experimental section (see Fig. 4 and 5).

Among the materials studied, potassium titanyl phosphate (KTP)[14] is used as a reference, which is one of the strongest SHG materials, and its intensity is approximately twice that of monoclinic (MelH)$ZnCl_3$(Mel). Nevertheless, the SHG signal of the monoclinic phase remains within the same order of magnitude as that of KTP, which is widely used as a benchmark material in nonlinear optics.

The SHG intensity of monoclinic (MelH)$ZnCl_3$(Mel) is about 1.5 times greater than that of orthorhombic (MelH)$ZnBr_3$(Mel). This is consistent with the theoretical expectation that lower-symmetry crystal systems generally allow a greater number of non-zero components in the second-order susceptibility tensor ($\chi^{(2)}$), thereby enhancing SHG efficiency.[15]

In addition, the orthorhombic bromide compound exhibits an SHG response approximately twice as strong as its chloride analogue. This increase can be attributed to the higher polarizability of bromide ions compared to chloride ions, which positively influences the overall nonlinear response.

The observed SHG efficiencies likely arise from a synergistic interplay between the polarizability of the Zn^{2+} centers, the halide ions, and the delocalized π-electron system of the melamine framework, all of which contribute to an increased second-order susceptibility.[16]

A quadratic dependence of SHG intensity on excitation power, as shown in Fig. 5, confirms the second-order nature of the process; linear regression of the logarithmically scaled data yields slopes close to 2, consistent with second-harmonic generation. Additionally, the presence of spectral peaks at wavelengths corresponding to half the excitation wavelength provides clear evidence that the observed signals originate from second harmonic generation.

These results confirm the second-order origin of the SHG signals and highlight the potential of zinc halide–melamine complexes as promising candidates for nonlinear optical applications such as frequency conversion.

Diffuse reflectance UV/Vis (DRUV) spectroscopy

Diffuse reflectance UV/Vis spectroscopy was performed for the phase-pure orthorhombic (MelH)$ZnBr_3$(Mel) (Fig. 6). The spectrum exhibits two broad absorption bands, which are assigned to the π → π* and n → π* transitions of the aromatic triazine ring system.[17] Compared to pure melamine, a hypsochromic

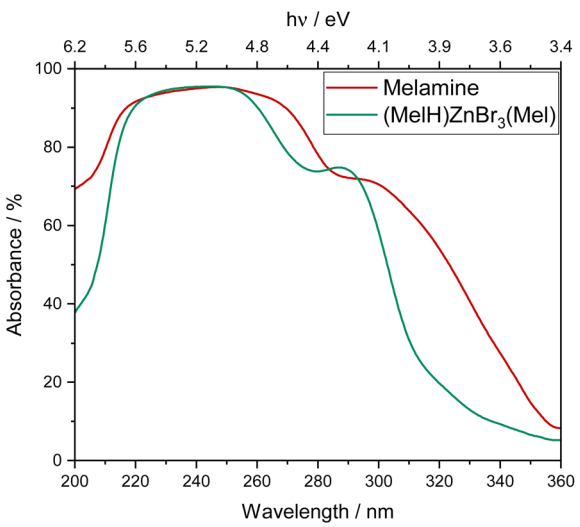

Fig. 6 Diffuse reflectance UV/Vis spectra of melamine (red) and orthorhombic (MelH)$ZnBr_3$(Mel) (green). Absorbance (%, left axis) is shown as a function of wavelength (nm) and photon energy (eV).

shift is observed, which can be attributed to the coordination of the melamine nitrogen atoms to Zn^{2+} and additional protonation at the ring nitrogen. These interactions modify the electronic structure and shift the π-system transitions to higher energies.[18]

The optical band gap was determined using a Tauc plot, yielding a direct band gap of 4.74 eV and an indirect band gap of 4.46 eV (Fig. 7).[19] Both values lie in the UV range, consistent with the observed formation of transparent, block-shaped crystals.

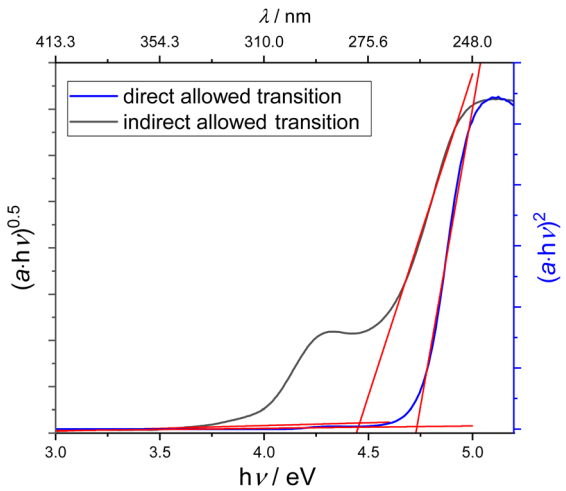

Fig. 7 Tauc plots from diffuse reflectance UV/Vis spectroscopy of orthorhombic $(C_3N_6H_7)ZnBr_3(C_3N_6H_6)$ showing the direct (blue) and indirect (black) transitions, with the corresponding linear fits in red.

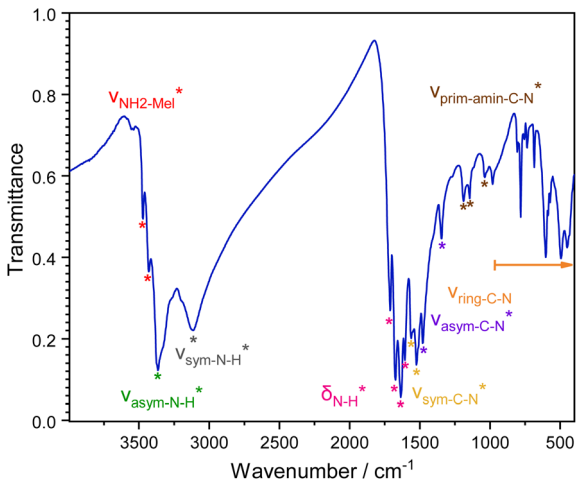

Fig. 8 Infrared spectrum of orthorhombic (MelH)$ZnBr_3$(Mel) with band assignments of characteristic vibrational modes.

Infrared (IR) spectroscopy

The infrared spectrum of orthorhombic (MelH)$ZnBr_3$(Mel), shown in Fig. 8, is compared with that of the previously reported monoclinic chloride analogue (MelH)$ZnCl_3$(Mel).[8b] Assignments of the observed vibrational bands to characteristic stretching and deformation modes for both compounds are summarized in Table 2. The bromide complex exhibits an additional NH_2 stretching band at 3555 cm^{-1}, characteristic of melamine.[20] Since melamine typically displays two bands in this region, the absence of the second band in the chloride complex may result from band overlap, background interference, or structural effects. One possible explanation is the presence of an extended hydrogen-bonding network in the orthorhombic bromide complex, whereas no such interactions are present in the monoclinic chloride analogue. This difference in hydrogen bonding may also account for the observed blue shift in the NH_2 stretching vibrations of the bromide complex.

Electronic structure

Density functional theory (DFT) was used to calculate the electronic band structure of orthorhombic (MelH)$ZnCl_3$(Mel) in order to understand the nature of the electronic states and chemical bonding in these materials. At the DFT level, orthorhombic (MelH)$ZnCl_3$(Mel) has a direct band gap at Γ (0 0 0) of 4.1 eV (see the SI), with nearly dispersionless valence and conduction bands, consistent with experimental results. The highest occupied bands are predominantly associated with nitrogen, whereas the lowest unoccupied bands are associated with carbon, indicating that the C–N π bonds in these materials play an important role in their optical properties. However, hybridized states with Zn and Cl character are also found beginning at 0.5 eV below the band gap, indicating that these components all contribute to the polarizable valence states.

Table 2 Assignment of the wavenumbers to the characteristic deformation and vibration oscillations in orthorhombic (MelH)$ZnBr_3$(Mel) and the published monoclinic (MelH)$ZnCl_3$(Mel)[8b]

Orthorhombic (MelH)$ZnBr_3$(Mel) Wavenumber/cm^{-1}	Monoclinic (MelH)$ZnCl_3$(Mel)	Assignment	
3555, 3539	3457	$\nu_{NH2-Mel}$	NH_2 stretching, typical of melamine
3472	3371	$\nu_{asym-N-H}$	Asymmetrical NH_2 stretching
3365	3140	$\nu_{sym-N-H}$	Symmetrical NH_2 stretching
1711–1607	1716–1645	δ_{N-H}	NH_2 deformation
1562, 1524	1525, 1482	$\nu_{sym-C-N}$	1,3,5-*s*-Triazine ring "quadrant stretching"
1479, 1346	1480, 1347	$\nu_{asym-C-N}$	1,3,5-*s*-Triazine ring "semicircle stretching"
1188–1038	1200–1050	$\nu_{prim-amin-C-N}$	C–N stretching, primary amines, tertiary C
982–449	779–459	$\nu_{ring-C-N}$	1,3,5-*s*-Triazine ring, out-of-plane ring bending by "sextants"

Conclusions

The two-component zinc halide–melamine system was investigated by means of solvothermal synthesis and solid-state reactions, showing that this type of reaction can be easily performed to prepare compounds with potential SHG properties. We resolved the crystal structures of zinc halide–melamine compounds (MelH)ZnX_3(Mel) with X = Cl, Br, and investigated their optical spectra by means of DRUV and IR spectroscopy. (MelH)$ZnCl_3$(Mel) appears with two non-centrosymmetric modifications, orthorhombic and monoclinic. The monoclinic chloride polymorph corresponds to the phase reported in the literature, and an alternative solid-state synthesis was established to yield a phase-pure crystalline material. Single-crystal SHG measurements revealed an increasing SHG response following the sequence orthorhombic (Cl) > orthorhombic (Br) > monoclinic (Cl). In the case of the orthorhombic chloride and bromide compounds, the presence of Br roughly doubles the response, consistent with increasing halide polarizability. These results indicate that heavier halides strengthen the second-order response for isotypic structures, and symmetry lowering can lead to further amplification. Guided by this trend, the monoclinic iodine analogue (MelH)ZnI_3(Mel) could deliver SHG intensities comparable to the benchmark SHG material KTP.

Experimental section

Melamine hydrohalides ($(C_3N_6H_6)HX$ with X = Cl, Br)

The melamine hydrohalides were synthesized according to the literature[21] by adding to a suspension of melamine (5.0 g, 3.96 mmol, 1 eq.) in deionized water (250 ml) at room temperature, followed by the addition of the corresponding concentrated acids HCl (40.0 ml, 47.6 mmol, 12 eq.); HBr (26.1 ml, 47.6 mmol, 12 eq.)). The mixtures were stirred overnight, filtered, and washed with 50 ml of deionized water. The resulting products were dried overnight at 80 °C. In all cases, a white powder was obtained.

Synthesis of $Zn_3(OH)_2Cl_4(C_3N_6H_6)_3$ and orthorhombic $(C_3N_6H_7)ZnCl_3(C_3N_6H_6)$

Hydrothermal synthesis was employed to produce both crystalline and powdered materials. $ZnCl_2$ (649 mg, 5.14 mmol, Sigma-Aldrich, ≥99.5%) and melamine (351 mg, 2.57 mmol, Sigma-Aldrich, 99.9%) were dissolved in 5 ml of double distilled and degassed water. The reaction mixture was enclosed in a Teflon-lined autoclave (volume = 15 ml) and heated slowly at a rate of 0.1 K min^{-1} to 110 °C and maintained at this temperature for 24 hours before cooling to room temperature at a rate of 0.1 K min^{-1}. The resulting crystals and powder (yield 15%) were air-dried at 80 °C. Despite variations in the reaction conditions, the formation of $Zn_3(OH)_2Cl_4(C_3N_6H_6)_3$ (yield 85%) could not be further minimized in this synthesis, preventing the isolation of pure orthorhombic $(C_3N_6H_7)ZnCl_3(C_3N_6H_6)$. Crystals of both compounds could be well distinguished, because they formed large plates and rods.

Synthesis of monoclinic $(C_3N_6H_7)ZnCl_3(C_3N_6H_6)$

In addition to the previously reported hydrothermal synthesis,[8b] this compound was prepared by a solid-state reaction of $ZnCl_2$ (321 mg, 2.35 mmol, 1 eq.), melamine hydrochloride (383 mg, 2.35 mmol, 1 eq.), and melamine (296 mg, 2.35 mmol, 1 eq.). The mixture was ground with an agate mortar to afford a homogeneous mixture and then sealed into a quartz ampoule. The ampoule was heated at a rate of 0.1 K min^{-1} to 120 °C and maintained at this temperature for 14 days, followed by cooling to room temperature at a rate of 0.1 K min^{-1}. A white crystalline powder was obtained in a quantitative yield (>95%).

Synthesis of $(C_3N_6H_7)ZnBr_3(C_3N_6H_6)$

A hydrothermal synthesis was employed to produce the crystalline material, aiming to optimize the crystal quality. $ZnBr_2$ (757 mg, 3.86 mmol, Sigma-Aldrich, ≥99.5%) and melamine (343 mg, 1.93 mmol, Sigma-Aldrich, 99.9%) were dissolved in 5 ml of double distilled and degassed water. The reaction mixture was enclosed in a Teflon-lined autoclave (volume = 15 ml) and heated slowly at a rate of 0.1 K min^{-1} to 110 °C where it was maintained for 24 hours, before cooling to room temperature at a rate of 0.1 K min^{-1}. The resulting crystals and powder (yield >95%) were dried in air at 80 °C.

Powder X-ray diffraction (PXRD)

PXRD patterns of the products were collected with a Stadi-P (STOE, Darmstadt) powder diffractometer using germanium monochromated Cu-$K_{\alpha1}$ radiation (λ = 1.5406 Å) and a Mythen 1K detector.

Single-crystal X-ray diffraction (SC-XRD)

SC-XRD studies were performed using a Rigaku XtaLAB Synergy-S diffractometer equipped with a HyPix 6000HE detector using CuK_α radiation (λ = 1.54184 Å) at 150 K. The structure was solved with the ShelXT 2018/2 solution program using dual methods and by using Olex2 1.5 as the graphical interface. The models were refined with ShelXL 2018/3 using full matrix least squares minimization on F^2 and Olex.refine with NoSphereA2.[22] All structural models were examined using PLATON to assess for overlooked higher symmetry; however, no missed symmetry elements were detected.[23]

Second harmonic generation (SHG) measurements

To perform the SHG measurements, the crystalline samples were put onto silicon wafers. The samples prepared this way could then be placed in a home-built parabolic mirror confocal microscope and the spectra and images could be collected. The ability of the microscope to measure a wide range of samples has been demonstrated in prior works.[24] A laser with a wavelength of 779 nm and a repetition rate of 80 MHz (FemtoFiber pro, Toptica Photonics) was used for the exci-

tation of individual crystals. A strict Gaussian beam with linear polarization was ensured through the use of a Glan–Taylor polarizer in the beam path. Both the focusing of the laser beam and the collection of the emitted signal were done through the use of a parabolic mirror, with a NA of 0.9986 in air. The scattered laser signal, as well as potentially the two-photon-photoluminescence, was blocked using a combination of a short pass filter with a filter wavelength of 750 nm and a bandpass filter with a range of 380 to 400 nm (nominal center wavelength of 390 nm). For samples, spatial intensity distribution images could be recorded using a high-precision nano-positioning stage (nPoint) where the intensity of each pixel was then collected using an avalanche photodiode. The filtered SHG spectra were then collected with a spectrometer with a 150 grooves per mm grating (Princeton Instruments) leading to a Pixis 100 charge-coupled device (Princeton Instruments).

Diffuse reflectance UV/Vis (DRUV) spectroscopy

The DRUV spectra were acquired using a Maya2000 Pro spectrometer (Ocean Optics) coupled to a Praying Mantis sample chamber (Harrick) and a DH-2000-BAL deuterium–tungsten lamp (Ocean Optics) as the illumination source. Data collection was performed using OceanView 1.6.7 Lite (Ocean Optics) under the following settings: 40 scans averaged, a boxcar width of 10, and an integration time of 30 ms. The bandgap E_g of (MelH)$ZnBr_3$(Mel) was calculated using the following equation: $(\alpha h\nu)^{1/n} = A(h\nu - E_g)$, where α is the absorption coefficient, h is the Planck constant, A is a material related constant and $h\nu$ is the photon energy. For an indirect allowed bandgap transition, the exponent $n = 2$ and for a direct allowed bandgap transition $n = 0.5$.[19]

Infrared (IR) spectroscopy

IR spectra were collected on a Bruker VERTEX 70 spectrometer in the range of 4000–400 cm^{-1}. Samples were prepared as KBr pellets inside a glovebox, pressed under ambient conditions, and subsequently stored under an inert atmosphere until measurement.

Density functional theory (DFT) calculations

DFT calculations were performed using the ABINIT software package (v.10).[25] The calculations were performed using a plane wave basis set and the PAW method,[26] with an energy cut-off of 26 Ha used outside the PAW spheres and 104 Ha inside. A 4 × 4 × 4 Monkhorst–Pack grid[27] of k-points was used to sample reciprocal space. These quantities were chosen following convergence studies, with the convergence criterion being 1% of the pressure. The Perdew–Burke–Ernzerhof exchange–correlation functional was used with the dispersion correction of Grimme.[28] PAW data files were used as received from the ABINIT library. The structures were relaxed to an internal pressure of 5 MPa prior to calculations of the electronic band structure.

Conflicts of interest

There are no conflicts to declare.

Data availability

The data that support the findings of this study are available in the supplementary information (SI) of this article. Supplementary information is available. See DOI: https://doi.org/10.1039/d5dt02245b. Computational data are availiable from DOI: https://doi.org/10.5281/zenodo.17613259.

CCDC 2478821, 2407677, 2438541 and 2407380 contain the supplementary crystallographic data for this paper.[29a–d]

Acknowledgements

The support for this research from the Deutsche Forschungsgemein-schaft (Bonn) through the project ME 914/34-1 and through the bwHPC project sponsored by the state of Baden-Württemberg and the German Research Foundation (DFG) through grant no. INST 40/467-1 FUGG (JUSTUS cluster) is gratefully acknowledged. C. P. R. acknowledges the support from the project FerrMion of the Ministry of Education, Youth and Sports, Czech Republic, co-funded by the European Union (CZ.02.01.01/00/22_008/0004591). We thank Peter Janoschek for performing the DRUV measurements.

References

1 (*a*) P. F. Bordui and M. M. Fejer, *Annu. Rev. Mater. Sci.*, 1993, **23**, 321–379; (*b*) P. Sangeetha, P. Jayaprakash, M. Nageshwari, C. R. T. Kumari, S. Sudha, M. Prakash, G. Vinitha and M. L. Caroline, *Phys. B*, 2017, **525**, 164–174; (*c*) Z. Qin, Y. Wen, Y. Shang, Y. Song and Y. Wan, *Appl. Phys. A*, 2007, **87**, 277–280; (*d*) S. K. Yesodha, C. K. S. Pillai and N. Tsutsumi, *Prog. Polym. Sci.*, 2004, **29**, 45–74; (*e*) S. Ahmed, X. Jiang, C. Wang, U. e. Kalsoom, B. Wang, J. Khan, Y. Muhammad, Y. Duan, H. Zhu and X. Ren, *Adv. Opt. Mater.*, 2021, **9**, 2001671; (*f*) X. Liu, Q. Guo and J. Qiu, *Adv. Mater.*, 2017, **29**, 1605886; (*g*) L. R. Dalton, A. W. Harper, R. Ghosn, W. H. Steier, M. Ziari, H. Fetterman, Y. Shi, R. Mustacich, A.-Y. Jen and K. J. Shea, *Chem. Mater.*, 1995, **7**, 1060–1081.

2 P. A. Franken, A. E. Hill, C. W. Peters and G. Weinreich, *Phys. Rev. Lett.*, 1961, **7**, 118–119.

3 (*a*) X. Meng, H. Tian, Q. Wu and M. Xia, *J. Cryst. Growth*, 2024, **648**, 127930; (*b*) X. Meng, W. Yin and M. Xia, *Coord. Chem. Rev.*, 2021, **439**, 213916; (*c*) J. Lu, Y.-K. Lian, L. Xiong, Q.-R. Wu, M. Zhao, K.-X. Shi, L. Chen and L.-M. Wu, *J. Am. Chem. Soc.*, 2019, **141**, 16151–16159; (*d*) F. Liang, L. Kang, X. Zhang, M.-H. Lee, Z. Lin and Y. Wu, *Cryst. Growth Des.*, 2017, **17**, 4015–4020.

4 (*a*) M. Kalmutzki, M. Ströbele, F. Wackenhut, A. J. Meixner and H. J. Meyer, *Inorg. Chem.*, 2014, **53**, 12540–12545;

(*b*) M. Kalmutzki, M. Ströbele, F. Wackenhut, A. J. Meixner and H. J. Meyer, *Angew. Chem., Int. Ed.*, 2014, **53**, 14260–14263.

5 (*a*) C. Dirk, R. Twieg and G. Wagniere, *J. Am. Chem. Soc.*, 1986, **108**, 5387–5395; (*b*) J. Chen, C.-L. Hu, F. Kong and J.-G. Mao, *Acc. Chem. Res.*, 2021, **54**, 2775–2783.

6 L. Vella-Zarb, D. Braga, A. G. Orpen and U. Baisch, *CrystEngComm*, 2014, **16**, 8147–8159.

7 (*a*) E. Bayat, M. Ströbele, M. Abbasi, S. Kroeker, J. Valenta, D. Enseling, T. Jüstel and H.-J. Meyer, *Inorg. Chem.*, 2024, **63**, 19053–19062; (*b*) E. Bayat, M. Ströbele, D. Enseling, T. Jüstel and H.-J. Meyer, *Molecules*, 2024, **29**, 5598; (*c*) A. B. Wiles, D. Bozzuto, C. L. Cahill and R. D. Pike, *Polyhedron*, 2006, **25**, 776–782.

8 (*a*) Z. Bai, J. Lee, H. Kim, C.-L. Hu and K. M. Ok, *Small*, 2023, **19**, 2301756; (*b*) L. Liu, Z. Bai, L. Hu, D. Wei, Z. Lin and L. Zhang, *J. Mater. Chem. C*, 2021, **9**, 7452–7457.

9 (*a*) M. Kompitsas, C. Baharis and Z. Pan, *J. Opt. Soc. Am. B*, 1994, **11**, 697–702; (*b*) D. Goebel, U. Hohm and G. Maroulis, *Phys. Rev. A*, 1996, **54**, 1973.

10 (*a*) D. Szunyogh, B. Gyurcsik, F. H. Larsen, M. Stachura, P. W. Thulstrup, L. Hemmingsen and A. Jancsó, *Dalton Trans.*, 2015, **44**, 12576–12588; (*b*) X.-L. Wang, Y.-F. Bi, G.-C. Liu, H.-Y. Lin, T.-L. Hu and X.-H. Bu, *CrystEngComm*, 2008, **10**, 349–356; (*c*) A. Erxleben, *Coord. Chem. Rev.*, 2003, **246**, 203–228; (*d*) H. Lopez-Sandoval, M. E. Londono-Lemos, R. Garza-Velasco, I. Poblano-Meléndez, P. Granada-Macías, I. Gracia-Mora and N. Barba-Behrens, *J. Inorg. Biochem.*, 2008, **102**, 1267–1276; (*e*) A. W. Kleij, M. Kuil, D. M. Tooke, A. L. Spek and J. N. Reek, *Inorg. Chem.*, 2005, **44**, 7696–7698.

11 (*a*) A. Zawadzka, P. Płóciennik, J. Strzelecki and B. Sahraoui, *Opt. Mater.*, 2014, **37**, 327–337; (*b*) K. Waszkowska, O. Krupka, O. Kharchenko, V. Figà, V. Smokal, N. Kutsevol and B. Sahraoui, *Appl. Nanosci.*, 2020, **10**, 4977–4982; (*c*) L.-Y. Wang, B.-Y. Shi, C.-B. Yao, Z.-M. Wang, X. Wang, C.-H. Jiang, L.-F. Feng and Y.-L. Song, *ACS Appl. Nano Mater.*, 2023, **6**, 9975–10014.

12 F. Jones, H. Tran, D. Lindberg, L. Zhao and M. Hupa, *Energy Fuels*, 2013, **27**, 5663–5669.

13 M. Kalmutzki, M. Ströbele, F. Wackenhut, A. J. Meixner and H.-J. Meyer, *Inorg. Chem.*, 2014, **53**, 12540–12545.

14 (*a*) J. D. Bierlein and H. Vanherzeele, *J. Opt. Soc. Am. B*, 1989, **6**, 622–633; (*b*) M. N. Satyanarayan, A. Deepthy and H. L. Bhat, *Crit. Rev. Solid State Mater. Sci.*, 1999, **24**, 103–191.

15 (*a*) A. Aghigh, S. Bancelin, M. Rivard, M. Pinsard, H. Ibrahim and F. Légaré, *Biophys. Rev.*, 2023, **15**, 43–70; (*b*) S. Ghimire and D. A. Reis, *Nat. Phys.*, 2019, **15**, 10–16; (*c*) F. Simon, S. Clevers, V. Dupray and G. Coquerel, *Chem. Eng. Technol.*, 2015, **38**, 971–983; (*d*) E. V. Kazantseva and A. I. Maimistov, *Opt. Spectrosc.*, 2000, **89**, 772–782.

16 H. Jia, X. Hou and S. Pan, *Inorg. Chem. Front.*, 2024, **11**, 7756–7774.

17 S. A. Kalyan, S. Elangovan, R. Karthick, N. Kanagathara, M. K. Marchewka and J. Janczak, *J. Mater. Sci.: Mater. Electron.*, 2024, **35**, 2100.

18 (*a*) L. Hynes, G. Montiel, A. Jones, D. Riel, M. Abdulaziz, F. Viva, D. Bonetta, A. Vreugdenhil and L. Trevani, *Mater. Adv.*, 2020, **1**, 262–270; (*b*) H. M. Vinusha, S. P. Kollur, H. D. Revanasiddappa, R. Ramu, P. S. Shirahatti, M. N. Nagendra Prasad, S. Chandrashekar and M. Begum, *Results Chem.*, 2019, **1**, 100012.

19 (*a*) J. Tauc, *Mater. Res. Bull.*, 1968, **3**, 37–46; (*b*) J. Tauc, *Amorphous and Liquid Semiconductors*, Springer, New York, 1974; (*c*) N. F. Mott and E. A. Davis, *Electronic processes in non-crystalline materials*, Oxford University Press, 2012; (*d*) A. R. Zanatta, *Sci. Rep.*, 2019, **9**, 11225; (*e*) Ł. Haryński, A. Olejnik, K. Grochowska and K. Siuzdak, *Opt. Mater.*, 2022, **127**, 112205; (*f*) J. Klein, L. Kampermann, B. Mockenhaupt, M. Behrens, J. Strunk and G. Bacher, *Adv. Funct. Mater.*, 2023, **33**, 2304523; (*g*) P. Y. Yu and M. Cardona, *Fundamentals of semiconductors. Physics and materials properties*, Springer, Berlin, Germany, 4th edn, 2010; (*h*) G. Kortüm and H. Koffer, *Ber. Bunsenges. Phys. Chem.*, 1963, **67**, 67–75; (*i*) G. Kortum and J. E. Lohr, *Reflectance Spectroscopy*, Springer My Copy UK, 1969; (*j*) M. P. Fuller and P. R. Griffiths, *Anal. Chem.*, 1978, **50**, 1906–1910; (*k*) A. B. Murphy, *Sol. Energy Mater. Sol. Cells*, 2007, **91**, 1326–1337; (*l*) R. López and R. Gómez, *J. Sol-Gel Sci. Technol.*, 2012, **61**, 1–7; (*m*) Z. M. Gibbs, A. LaLonde and G. J. Snyder, *New J. Phys.*, 2013, **15**, 075020; (*n*) P. Makuła, M. Pacia and W. Macyk, *J. Phys. Chem. Lett.*, 2018, **9**, 6814–6817; (*o*) G. D. Gesesse, A. Gomis-Berenguer, M.-F. Barthe and C. O. Ania, *J. Photochem. Photobiol., A*, 2020, **398**, 112622.

20 X. Yuan, K. Luo, K. Zhang, J. He, Y. Zhao and D. Yu, *J. Phys. Chem. A*, 2016, **120**, 7427–7433.

21 (*a*) J. Barrio and M. Shalom, *Mater. Sci. Semicond. Process.*, 2018, **73**, 78–82; (*b*) G. Bertelli, G. Camino, L. Costa and R. Locatelli, *Polym. Degrad. Stab.*, 1987, **18**, 225–236.

22 (*a*) *CrysAlisPro Software System*, Rigaku Oxford Diffraction, 2024; (*b*) O. V. Dolomanov, L. J. Bourhis, R. J. Gildea, J. A. K. Howard and H. Puschmann, *J. Appl. Crystallogr.*, 2009, **42**, 339–341; (*c*) G. Sheldrick, *Acta Crystallogr., Sect. C: Struct. Chem.*, 2015, **71**, 3–8; (*d*) G. Sheldrick, *Acta Crystallogr., Sect. A: Found. Adv.*, 2015, **71**, 3–8; (*e*) G. Sheldrick, *Acta Crystallogr., Sect. A: Found. Crystallogr.*, 2008, **64**, 112–122; (*f*) L. J. Bourhis, O. V. Dolomanov, R. J. Gildea, J. A. K. Howard and H. Puschmann, *Acta Crystallogr., Sect. A: Found. Adv.*, 2015, **71**, 59–75; (*g*) F. Kleemiss, O. V. Dolomanov, M. Bodensteiner, N. Peyerimhoff, L. Midgley, L. J. Bourhis, A. Genoni, L. A. Malaspina, D. Jayatilaka, J. L. Spencer, F. White, B. Grundkötter-Stock, S. Steinhauer, D. Lentz, H. Puschmann and S. Grabowsky, *Chem. Sci.*, 2021, **12**, 1675–1692.

23 A. Spek, *J. Appl. Crystallogr.*, 2003, **36**, 7–13.

24 (*a*) J. Wang, J. Butet, G. D. Bernasconi, A.-L. Baudrion, G. Lévêque, A. Horrer, A. Horneber, O. J. Martin, A. J. Meixner and M. Fleischer, *Nanoscale*, 2019, **11**, 23475–23481; (*b*) E. Gürdal, A. Horneber, A. J. Meixner, D. P. Kern, D. Zhang and M. Fleischer, *Nanoscale*, 2020, **12**, 23105–23115; (*c*) L. Pan, P. Miao, A. Horneber, A. J. Meixner,

P.-M. Adam and D. Zhang, *Beilstein J. Nanotechnol.*, 2022, **13**, 572–581; (*d*) L. Pan, P. Miao, A. Horneber, A. J. Meixner, P.-M. Adam and D. Zhang, *ACS Appl. Nano Mater.*, 2023, **6**, 6467–6473; (*e*) J. P. Wang, Y. Q. Fang, W. He, Q. Liu, J. R. Fu, X. Y. Li, Y. Liu, B. Gao, L. Zhen and C. Y. Xu, *Adv. Opt. Mater.*, 2023, **11**, 2300031; (*f*) R. Wang, Q. Liu, S. Dai, C. M. Liu, Y. Liu, Z. Y. Sun, H. Li, C. J. Zhang, H. Wang and C. Y. Xu, *Small*, 2024, **20**, 2305658.

25 M. J. Verstraete, J. Abreu, G. E. Allemand, B. Amadon, G. Antonius, M. Azizi, L. Baguet, C. Barat, L. Bastogne and R. Bejaud, *arXiv*, 2025, preprint, arXiv:2507.08578, DOI: 10.48550/arXiv.2507.08578.

26 M. Torrent, F. Jollet, F. Bottin, G. Zérah and X. Gonze, *Comput. Mater. Sci.*, 2008, **42**, 337–351.

27 H. J. Monkhorst and J. D. Pack, *Phys. Rev. B*, 1976, **13**, 5188–5192.

28 (*a*) J. P. Perdew, K. Burke and M. Ernzerhof, *Phys. Rev. Lett.*, 1997, **78**, 1396–1396; (*b*) S. Grimme, J. Antony, S. Ehrlich and H. Krieg, *J. Phys. Chem.*, 2010, **132**, 154104.

29 (*a*) CCDC 2478821: Experimental Crystal Structure Determination, 2025, DOI: 10.5517/ccdc.csd.cc2p6dz9; (*b*) CCDC 2407677: Experimental Crystal Structure Determination, 2025, DOI: 10.5517/ccdc.csd.cc2ltd0v; (*c*) CCDC 2438541: Experimental Crystal Structure Determination, 2025, DOI: 10.5517/ccdc.csd.cc2mvhmm; (*d*) CCDC 2407380: Experimental Crystal Structure Determination, 2025, DOI: 10.5517/ccdc.csd.cc2lt2fy.